J. Fluid Mech. (1990), *vol.* 218, *pp.* 439–461
Printed in Great Britain

Spatial organization of large structures in the turbulent far wake of a cylinder

By D. K. BISSET, R. A. ANTONIA AND L. W. B. BROWNE
Department of Mechanical Engineering, University of Newcastle, NSW, 2308, Australia

(Received 9 February 1988 and in revised form 15 February 1990)

Using an array of ×-probes aligned in the plane of mean shear in the turbulent far wake of a circular cylinder, instantaneous velocity vector patterns are obtained from which stream-function approximations and sectional streamlines are derived. Conditional patterns obtained using different methods for detecting the organized motion are essentially independent of the particular method used. The spatial arrangement of the organized motion about the flow centreline varies in a continuous manner between opposing and alternating modes, the latter being nearly twice as common as the former. Results presented include conditional patterns for the opposing and alternating modes and the relative contributions made by each mode to the Reynolds stresses. A modified Rankine vortex kinematic model, based as much as possible on experimental data and incorporating both modes, yields mean velocity and Reynolds stress distributions which agree well with experiment. A quasi-three-dimensional version of the model implies that large spanwise vortices and shear-aligned double rollers represent the same three-dimensional organized motion from two different viewpoints.

1. Introduction

Flow visualizations (e.g. Taneda 1959; Papailiou & Lykoudis 1974; Wlezien 1981; Cimbala 1984, 1985) and hot-wire measurements (e.g. Grant 1958; Townsend 1979; Mumford 1983; Browne, Antonia & Bisset 1986; Ferré i Vidal 1986) in the turbulent far wake of a circular cylinder have highlighted the existence of large-scale organized motions often alternating about the centreline. The primary vortex street is usually of the Kármán type, although observations of symmetrically arranged vortices have been reported in the near wake (e.g. Wygnanski, Champagne & Marasli 1986). In the far wake, the alternating arrangement seems to prevail, but the motion is much less regular than in the near wake. Wygnanski & Petersen (1987) have noted that the linear modes of instability in the wake are the same as in the plane jet (mean velocity profiles in both flows have two inflection points). The topological information obtained by Antonia *et al.* (1986) and the measurements of Oler & Goldschmidt (1981, 1982) and Thomas & Goldschmidt (1986) support the existence of an alternating pattern in the far field of the plane jet, as in the far wake.

There is flow visualization evidence (Keffer 1965; Antonia & Fulachier 1986), however, to suggest that the organized motion in the far wake is sometimes symmetrical, with vortices opposite each other across the centreline. Keffer (1965) attributed the lack of correlation between bulges on opposite sides of the centreline to the fact that they could be either alternately spaced or arranged symmetrically. This observation is also supported by photographs of dye streaklines (Antonia &

Fulachier 1986) in a water tunnel: streaklines introduced on opposite sides of the centreline in the far wake of a cylinder were usually deformed alternately about the centreline but symmetrical displacements of the streaklines were also observed to occur.

A linear inviscid instability analysis was carried out by Wygnanski *et al.* (1986) for the turbulent far wake, in which both sinuous and varicose modes of instability were considered. Computed streaklines and vorticity perturbation contours for each mode showed the expected behaviour but the results for the combination of the two modes looked more like those for the sinuous mode, thus highlighting the dominance of the sinuous instability, which has a slightly higher rate of amplification than the varicose mode. Wygnanski *et al.* (1986) also drew attention to the fact that the presence of the varicose mode not only modulates the streaklines but also contributes to an apparently chaotic motion, which is reflected in the observations.

Although there is abundant evidence of great variety of form and arrangement of large structures within flows such as the turbulent plane wake, much of the work to date has concerned the eduction of the strongest and most coherent structures (e.g. Hussain 1986; Antonia *et al.* 1986) arranged in the most probable way. For example, Browne, Antonia & Bisset (1986) depicted the topology of the organized motion in the far wake of a cylinder, relative to an observer translating at an appropriate velocity, by conditioning the data on spatially coherent temperature fronts which occurred alternately about the centreline with the most probable spacing. In the present paper the variety of spatial arrangements of large structures in the turbulent far wake of a cylinder is considered and quantified. An array of $\times$-wires, aligned in the plane of mean shear, allows the organized motion to be observed either instantaneously or conditionally. Two different methods of detecting the organized motion are used, and conditional results are presented for the opposing and alternating modes. The contributions from both these modes to the Reynolds stresses are compared. A numerical vortex model is developed which reproduces many of the characteristics of the experimental data such as Reynolds normal and shear stress profiles. Incorporation of the alternating and opposing modes is essential to the model. Although intended to be two-dimensional, the model implies a three-dimensional motion which, in planes parallel to the centreplane, could be interpreted as the double-roller structure of Grant (1958) and Mumford (1983).

Some of the experimental work for this paper was discussed previously in Antonia, Browne & Bisset (1987*a*).

2. Experimental details

The wind tunnel and cylinder have been described in Browne *et al.* (1986). Measurements were made in an open-return low-turbulence wind tunnel with a working section of 350 mm $\times$ 350 mm, 2.4 m long. The wake was generated by a cylinder of diameter $d = 2.67$ mm spanning the width of the working section. The bottom wall of the working section was adjusted to obtain a zero streamwise pressure gradient. The free-stream velocity U_1 was 6.7 m/s and the Reynolds number, based on U_1 and d, was 1170. All measurements were made at $x/d = 420$, where x is the streamwise distance measured from the cylinder. At this location, the mean velocity half-width L was 12.3 mm, and the mean centreline velocity defect U_0 was 0.36 m/s. Asterisked quantities are normalized by L and/or U_0.

The turbulence intensity at $x/d = 420$ varied from 1.6% on the centreline to a peak of 1.9% near L, decreasing to the free-stream value in the outer regions of the wake.

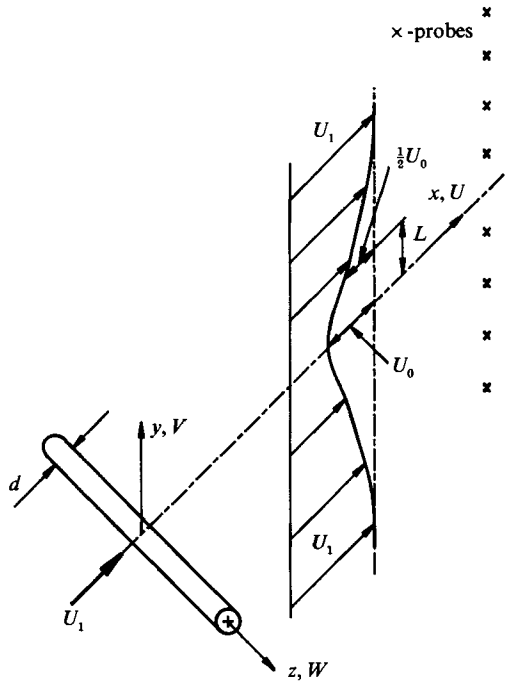

FIGURE 1. Definition sketch and experimental arrangement.

The present Reynolds number is significantly larger than the value of about 160 at which the wake is considered turbulent (Cimbala 1985; and Cimbala, Nagib & Roshko 1988). Evidence that the present flow has reached self-preservation is given in Browne & Antonia (1986). The advantage of this flow is that the Kolmogorov lengthscales are reasonably large (of the order of 0.4 mm) so that measurements may be made quite accurately with hot-wire probes. Nevertheless, the flow is fully turbulent (r.m.s. values of longitudinal and transverse velocity fluctuations are up to 33% and 25% of U_0 respectively, and spectra of fluctuations are broadbanded).

For the present experiment, an array of eight equispaced × -probes was aligned in the y or transverse direction, with four × -probes arranged on either side of the centreline, as shown in figure 1. Each × -probe provided velocity fluctuations u and v, in the x- and y-directions respectively, and adjacent probes were separated by 7.1 mm. The hot wires were operated at an overheat of 0.6 with constant-temperature anemometers built in-house. The signals from the anemometers were offset, amplified and then digitized using a 16 channel, 12 bit data acquisition system, at a sampling frequency of 3470 Hz per channel (filter cutoff frequency = 1750 Hz) into a PDP 11/34 computer. Using velocity and yaw calibrations, signals proportional to u and v were formed and stored on tape for a record duration of about 53 s. Mean velocities, $\bar{U}$, for each wire were obtained using a personal computer with a data-logging system connected directly to the output of each anemometer. Subsequent data processing was carried out on a VAX 11/780 computer.

3. Detection of organized motion

Browne *et al.* (1986) used the same set-up as for the present results except that the cylinder was electrically heated. They detected the organized motion by applying a

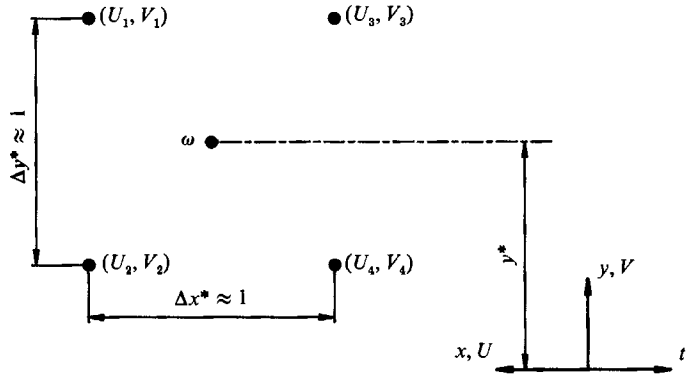

FIGURE 2. Computational scheme used in calculating the large-scale spanwise vorticity ω.

modified VITA procedure to temperature fluctuations, which acted as a passive marker of the motion or, more correctly, of a particular spatial feature of this motion. In the present work the velocity signals from the array of $\times$-wires are used for detection. Two basically different types of detection are used. The first is somewhat similar to that used by Hayakawa & Hussain (1985) in the near wake; it is based on detections of peaks in an approximation to the large-scale spanwise vorticity. The second focuses on sudden changes in the lateral velocity fluctuation v-signal. In this sense it is similar to the detection used in Browne *et al.* (1986) which focused on rapid, large-scale changes in the temperature signals. Here though, we do not use the modified VITA procedure.

3.1. *Detection using large-scale vorticity*

In this method, digital (u, v) signals from two $\times$-wires on the same side of the wake centreline are searched for positive or negative peaks in the large-scale spanwise vorticity. The approximation to the instantaneous spanwise vorticity is

$$\omega \approx \frac{\Delta V}{\Delta x} - \frac{\Delta U}{\Delta y},$$

where $U\ (= \bar{U} + u)$ and $V\ (= \bar{V} + v)$ are instantaneous signals formed by adding $\bar{U}(y)$ and $\bar{V}(y)$ to the digital time series of the fluctuations u and v, although $\bar{V}$ is negligibly small in the present case. To convert time separations into distances, we have used $\Delta x \equiv -U_c \Delta t$, where U_c is taken to be the mean velocity (6.5 m/s) at $y^* = 0.8$. Since it is assumed that the region of coherent vorticity for large structures is at least L in the x- and y-directions (it is greater than L for conditionally averaged structures (Antonia *et al.* 1987*a*)), Δx and Δy are chosen to be approximately equal to L, i.e. $\Delta x^* \approx \Delta y^* \approx 1$. Referring to figure 2, which shows the locations of four (U, V) data pairs, the instantaneous spanwise vorticity at the centre of the data points was calculated from

$$\omega = \frac{-1}{U_c \Delta t}[\tfrac{1}{2}(V_3 + V_4) - \tfrac{1}{2}(V_1 + V_2)] - \frac{1}{\Delta y}[\tfrac{1}{2}(U_1 + U_3) - \tfrac{1}{2}(U_2 + U_4)]. \quad (1)$$

It is more usual to use Taylor's hypothesis, viz. $\Delta x = -\bar{U}\Delta t$, for this conversion but in the present flow, the variation of $\bar{U}$ at $x/d = 420$ is only small (a maximum of 6%) so that the present conversion is essentially equivalent to Taylor's hypothesis.

One detection is recorded for each continuous patch of data for which $|\omega| > \beta_1$,

and ω is positive or negative depending on whether the signals are below or above the centreline respectively, where β_1 is a threshold value. The detection point is the instant at which $|\omega|$ is largest. Typical traces of ω are shown at the top and bottom of figure 3(*a*), with the computations centred at $y^* = 0.88$ and $y^* = -0.85$ respectively. Since there can be local high-frequency variations in ω, the threshold test is suspended for a short time after $|\omega|$ first exceeds or falls back below β_1; a suspension time of about one seventh of the average convection time of the structures was used. The value of β_1 was $0.87U_0/L$ for most of the present work, giving an average detection frequency approximately equal to the average structure frequency (determined from the peak in the spectrum of v), i.e. 125 Hz at $x/d = 420$. Detection positions are indicated by arrows in figure 3(*a*).

3.2. *Detection based on velocity fluctuation v*

A computation window of size $(2\tau+1)$ data points is moved point by point through the digital record of v-fluctuations, v_j, $j = 1,2,\ldots,N$, where N is the total number of data. The value of the WAG (window average gradient) at point j is calculated using

$$WAG_j = \frac{\text{sign}}{2\tau}\left[\sum_{i=j+1}^{j+\tau} v_i - \sum_{i=j-\tau}^{j-1} v_i\right],$$

where sign is equal to $+1$ or -1 (depending on whether v is measured below or above the flow centreline) to ensure that the value of the WAG is always positive for detections. Thus, detections above the centreline are based on sudden decreases in v while detections below the centreline are based on sudden increases in v.

A detection region begins when $\text{WAG}_j > \beta_2 v'$ first occurs (β_2 is some threshold value and v' the r.m.s. value of v), and ends when WAG < 0. The detection instant j_m within each detection region is the value of j for which WAG is largest. The size of the window $(2\tau+1)$ is not critical, but is set at about half the number of data points required to cover the period of the structures for which a search is being made. The minimum reasonable value of β_2 (typically 0.5 to 0.6) is that for which the average detection frequency is approximately equal to the average structure frequency.

The total number n of detections was typically about 7000 for both the large-scale vorticity and v-signal detection methods.

4. Conditional and structural averages

The conditional average, for n detections, of an instantaneous quantity F is given by

$$\langle F\rangle_k = \frac{1}{n}\sum_{m=1}^{n} F_{j_m+k}, \tag{2}$$

where k represents time (in samples, positive or negative) relative to the detection points j_m. The subscript k is generally omitted. Therefore

$$F = \langle F\rangle + f_r,$$

where f_r is the component of F not correlated with the detected large-scale motion. If $f \equiv F - \bar{F}$ is the instantaneous fluctuation,

$$f = \tilde{f} + f_r,$$

where $\tilde{f} \equiv \langle f \rangle$ is the fluctuation component due to the detected large-scale motion, and therefore

$$F = \bar{F} + \tilde{f} + f_r.$$

Also,
$$\langle fg \rangle = \tilde{f}\tilde{g} + \langle f_r g_r \rangle, \tag{3}$$

where f and g can each stand for either u or v.

If the conditionally averaged structure begins k_1 data points before the detection instant and ends k_2 data points after the detection instant, then we define the structure averages as

$$\overline{\langle fg \rangle} = \frac{1}{k_1 + k_2 + 1} \sum_{-k_1}^{k_2} \langle fg \rangle_k, \tag{4}$$

with similar expressions for the other terms of (3). Note that $\overline{\langle fg \rangle}$ will be very close to the conventional Reynolds stress $\overline{fg}$ if it is computed from structures that are reasonably representative of the flow.

5. Flow patterns obtained from the ×-wire array

The information obtained from the ×-wire array can be used without conditioning for 'visualizing' large-scale coherent patterns of the flow or, more correctly, a two-dimensional cross-section of these patterns in the plane of the array. Instantaneous velocity vectors are shown in figure 3(*a*) for a record duration of 18.4 ms. In figure 3 and subsequent figures the frame of reference is moving from right to left at a velocity $U_c = 6.52$ m/s ($\approx \bar{U}$ at $y^* = 1.0$), and $\Delta x = -U_c \Delta t$. The vectors are displayed in the $(\Delta x^*, y^*)$-plane and identical scales are used for Δx^* and y^*. In order to facilitate visual interpretation of the vector plots made from the eight ×-wires, two extra rows of vectors were interpolated between each pair of existing rows by fitting cubic polynomials in the y-direction to the measured U- (or V-) values. Such interpolated data make visual interpretation easier, and yet do not distort the picture suggested by the original data; eight of the 22 lines of vectors in figure 3(*a*) are the original vectors. The interpolated data were also used when obtaining all contour plots presented in this paper.

The instantaneous velocity vectors of figure 3(*a*) delineate a succession of rotational patterns on either side of the centreline. No smoothing has been applied to this figure and all vectors have been shown. The record duration used in figure 3(*a*) corresponds to a streamwise distance of about 2.5 average wavelengths. The patterns revealed in the figure occur at an average streamwise spacing which is in reasonable agreement with the most probable streamwise separation ($\Delta x^* \approx 3.4$) of temperature fronts (Browne *et al.* 1986).

Figure 3(*a*), which is quite typical of the whole record, reveals that there is a significant variation in the streamwise distance between consecutive critical points (defined as points where the velocity is zero and the streamline slope is indeterminate) of rotational patterns on either side of the centreline. The critical points in figure 3(*a*) are centres or foci, denoted by the letter C, and saddles, denoted by the letter S. Critical points correspond fairly closely to local extrema in the spanwise vorticity traces (figure 3*a*): below the centreline for example, centres/foci can be identified with maxima while saddle points are close to minima. Centres/foci on one side of the centreline usually occur opposite saddles on the opposite side of the centreline thus providing the generally alternating structure arrangement. For example, centres/foci at C_{2+} and C_{3+} (figure 3*a*; subscripts + and − refer to locations above and below the centreline) lie approximately opposite saddle points S_{2-} and S_{3-}. The structure with

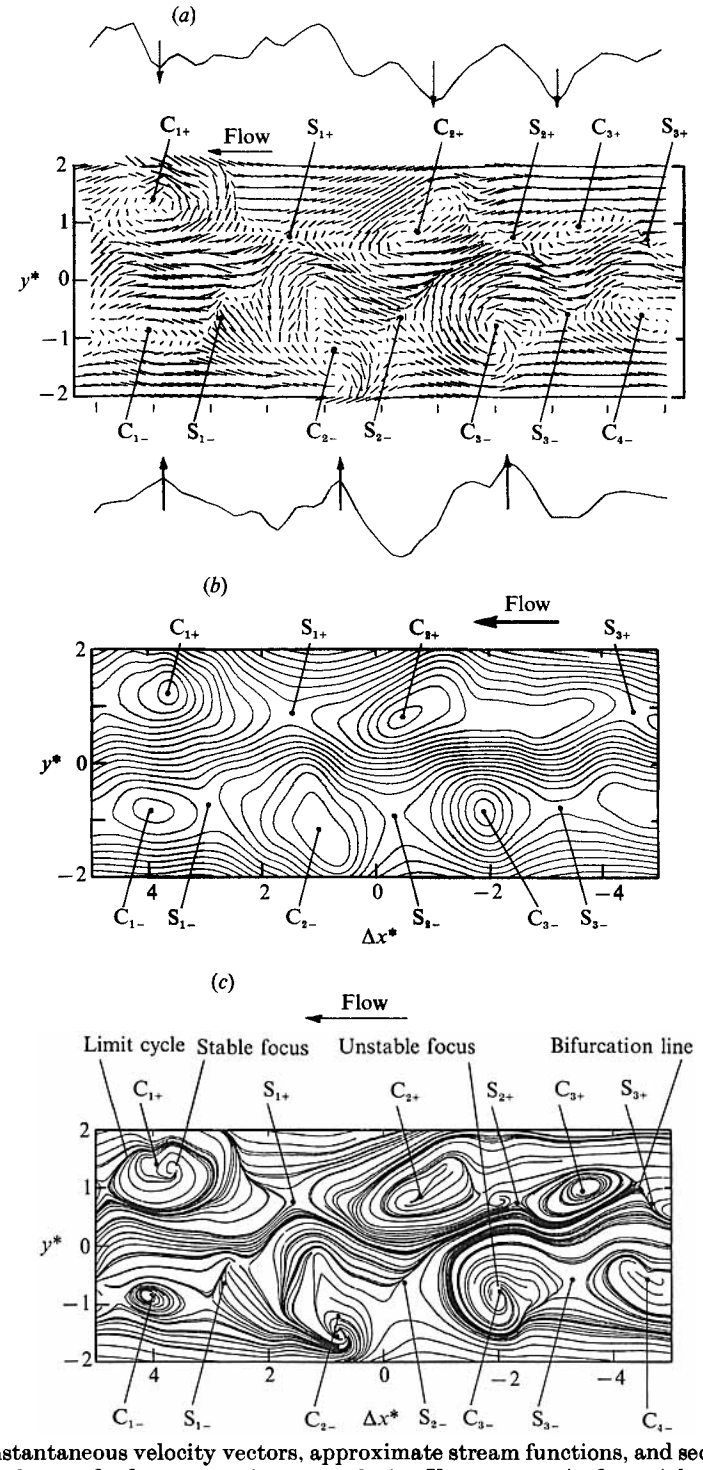

FIGURE 3. Instantaneous velocity vectors, approximate stream functions, and sectional streamlines observed in a frame of reference moving at a velocity U_c (= 6.52 m/s) from right to left. The record duration is 18.4 ms. C are centres/foci, S are saddles, subscripts + and − refer to positive and negative y-positions respectively. (*a*) Velocity vectors with traces of instantaneous large-scale vorticity centred at $y^* = 0.88$ (above) and $y^* = -0.85$ (below). (*b*) Equally spaced contours of two-dimensional approximate stream functions. (*c*) Sectional streamlines.

its centre/focus at C_{1+}, however, is nearly opposite C_{1-} below the centreline. Figure 3(*a*) also indicates some variation in the lateral distances from centres/foci and saddles to the centreline. We can also infer from figure 3(*a*) the possible interaction between neighbouring structures, as illustrated by the significant deformation of some of the patterns and the likely variability in the strength of the vortices associated with different patterns. These latter aspects of the organized motion are not addressed in this paper but should be worthy of future investigation.

Equally spaced contours of approximate two-dimensional stream functions which correspond to the instantaneous vectors of figure 3(*a*) are shown in figure 3(*b*). The divergence $\partial U/\partial x + \partial V/\partial y$ is not always zero, so the stream function ψ could not be calculated by direct numerical integration of the array of $[(U-U_c), V]$-values. An iterative procedure was therefore adopted: an initial estimate of ψ values was obtained by integration, and then $\partial\psi/\partial y$ was compared with $(U-U_c)$ for each data point and $-\partial\psi/\partial x$ was compared with V, and the values of ψ were adjusted until adequate convergence was achieved (see Appendix for details). Figure 3(*b*) generally allows the flow patterns to be seen more conveniently than figure 3(*a*), although it is evident that some critical points, S_{2+} and C_{3+}, are poorly defined (and therefore not shown) in figure 3(*b*).

Lines to which the velocity vectors are exactly tangential, i.e. sectional streamlines (see Perry & Chong 1987), can be found by numerically integrating the equation $\mathrm{d}\boldsymbol{r}/\mathrm{d}s = \boldsymbol{V}(\boldsymbol{r})$, where $\boldsymbol{r}$ is a fluid particle position vector and s is equivalent to time in the frozen frame of the velocity vectors. Thus

$$x = x_0 + \int_{t_0}^{t} U[x(s), y(s)] - U_c \,\mathrm{d}s, \tag{5a}$$

$$y = y_0 + \int_{t_0}^{t} V[x(s), y(s)] \,\mathrm{d}s. \tag{5b}$$

The algorithm for determining sectional streamlines from discrete velocity data is given in the Appendix. Figure 3(*c*) shows sectional streamlines corresponding to the vectors of figure 3(*a*). The topology presented is richer, in that stable and unstable foci, limit cycles, and bifurcation lines now appear. Unambiguous interpretation of this topology requires three-dimensional information about all three velocity components, however. The topology obtained with the stream-function approach can be viewed as the two-dimensional limiting case for mildly divergent data, while the topology revealed by sectional streamlines conveys more information but is more sensitive to the choice of convection velocity.

6. Occurrence of alternating and opposing modes

Velocity vector or streamline patterns similar to those in figure 3 tend to support, at least qualitatively, the idea that the alternating mode is prevalent. This can be illustrated by considering conditional averages from all eight $\times$-probes based on detections at only one y^* location. Stream functions derived from such conditional averages based on v-detections at $y^* = 0.9$ are shown in figure 4. The emerging pattern clearly emphasizes the dominance of the alternating mode. To quantify the importance of the alternating mode relative to the opposing mode, a study was made of the time relationships between detections in the signals from probes on opposite sides of the centreline. Curves of the relative probability of Δt (scaled to a maximum of 1.0) are shown in figure 5, where Δt is the time difference between detections at y^*

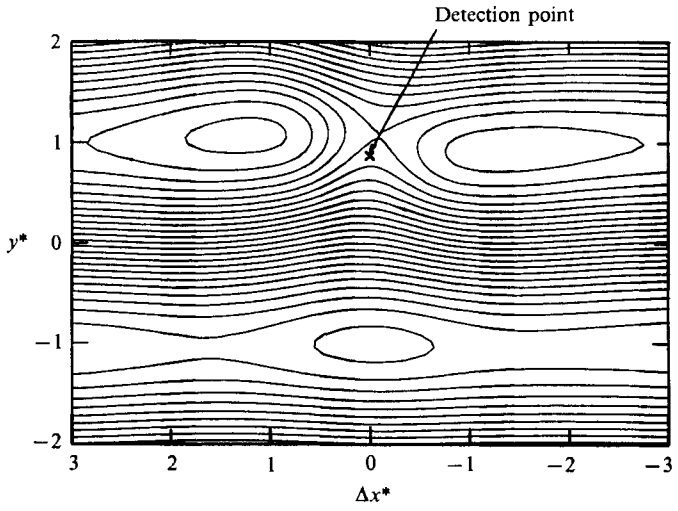

FIGURE 4. Equally spaced contours of conditionally averaged two-dimensional approximate stream functions obtained using the v-detection method applied at $y^* = 0.9$.

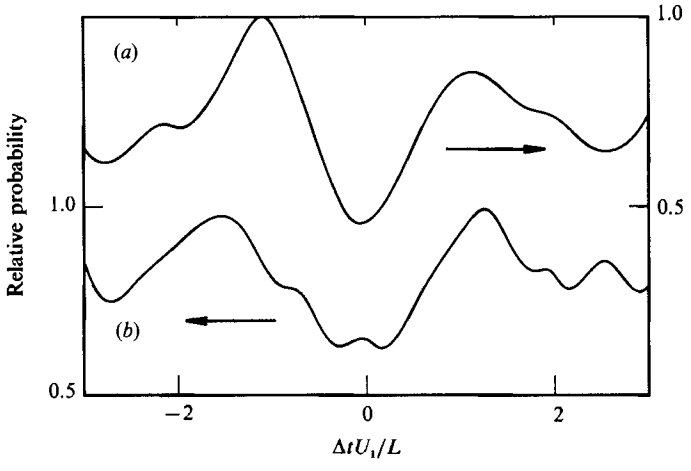

FIGURE 5. Relative probability of the duration between detections at $y^* = 0.9$ and $y = -0.9$ (reference location). (*a*) Vorticity detection method; (*b*) v-detection method.

$= +0.9$ and those at the reference position, $y^* = -0.9$. For both detection methods, the probability is a minimum at $\Delta t = 0$ and reaches local maxima at $\Delta t U_1/L \approx \pm 1.5$. Since the relative probability is in the range 0.5–0.6 at $\Delta t = 0$, the importance of the opposing mode cannot be ignored. As the distributions in figure 5 are continuous, all intermediate arrangements between opposing and alternating modes are possible. Results essentially similar to those in figure 5 were obtained for detections at several different y^* positions.

Subsets of detections were selected to illustrate: (i) the least probable case (opposite mode); and (ii) the most probable case (alternate mode) using the information of figure 5. In order to allow direct comparison of results for the alternating mode obtained with the two detection methods, the reference detection position was at $y^* = +0.9$ for the vorticity detection method and at $y^* = -0.9$ for the v-detection method. For (i), simultaneous detections were required at $y^* = -0.9$

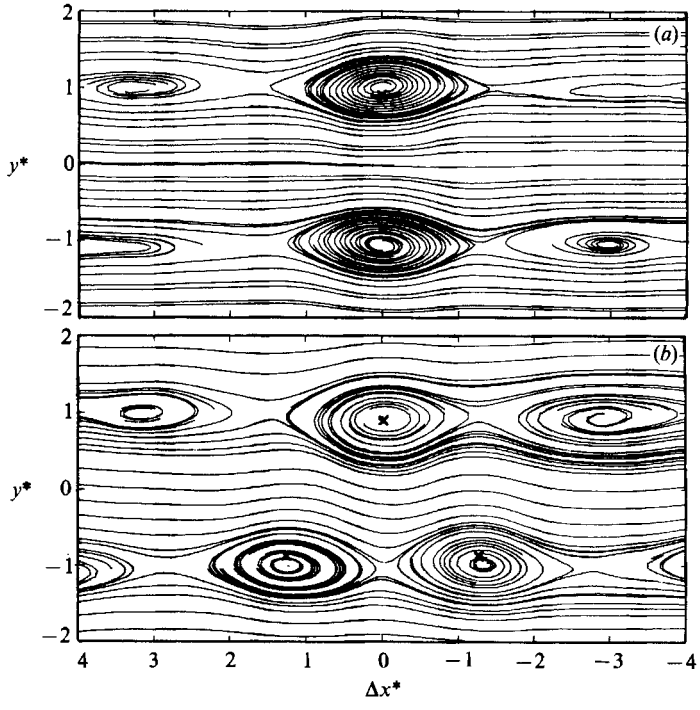

FIGURE 6. Sectional streamlines calculated from conditional averages obtained with the vorticity detection (reference location $y^* = 0.9$): ×, detection points. (*a*) Opposing mode; (*b*) exactly alternating mode.

and $y^* = 0.9$, and approximately 650 detection pairs were found. For (ii), detections were required at $\Delta t = 0$ for the reference location and at both $\Delta t\, U_1/L = -1.5$ and $\Delta t\, U_1/L = 1.5$ for the other y^* location. There were approximately 1130 detection pairs that satisfied the first time delay criterion ($\Delta t\, U_1/L = -1.5$), and 170 detection trios that satisfied both time delay criteria.

Sectional streamlines calculated from velocity vectors conditioned on each of the above detection subsets are shown in figures 6 (vorticity detection) and 7 (*v*-detection). It is of some importance to comment on the fundamental agreement between the patterns in figure 6(*a*) and those in figure 7(*a*) or that between the patterns in figure 6(*b*) and figure 7(*b*) because the detection methods used in obtaining these figures are appreciably different. The vorticity detection method focuses on points of maximum spanwise vorticity (centres or foci). By contrast, the *v*-detection method focuses on saddle points which, as noted earlier, are located on the diverging separatrix where the spanwise vorticity is lowest. Temperature fronts are aligned approximately with the diverging separatrix and it is therefore not surprising that the patterns obtained (Browne *et al.* 1986; Antonia *et al.* 1987*b*) on the basis of temperature front detections are in good agreement with those obtained using the *v*-detection. Hussain (1983, 1986) has stated that coherent structures are least ambiguously defined in terms of vorticity so that the trigger for educing the structures should be based on the instantaneous vorticity signal. This constraint may be too restrictive, because the flow topology of the organized motion should comprise the essential characteristics of the flow physics, and consequently, a detection

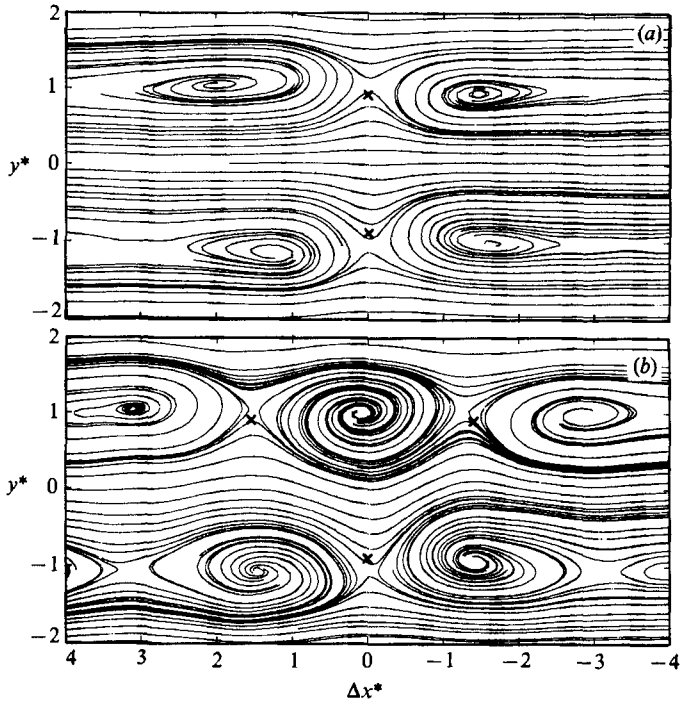

FIGURE 7. Sectional streamlines calculated from conditional averages obtained with the v-detection (reference position $y^* = -0.9$): ×, detection points. (*a*) Opposing mode; (*b*) exactly alternating mode.

method which focuses on saddle points or diverging separatrices should be as valid as one which searches for concentrations of spanwise vorticity.

In figure 8(*a*) contours of spanwise vorticity $\omega^* = \Delta V^*/\Delta x^* - \Delta U^*/\Delta y^*$, calculated with (1) but now with the smallest possible Δx^* (≈ 0.15) and Δy^* (≈ 0.18 for the interpolated data) are presented for the same instantaneous data as in figure 3. The region between the saddles S_{1-} and S_{2-} appears as a single distorted structure in vector, stream function and sectional streamline plots, but contains two quite distinct peaks of vorticity in figure 8(*a*). This structure could be the result of a recent merger between two smaller structures (although there are other reasonable explanations), but in any case it highlights structure variability, a problem which must be addressed in all detection schemes.

Contours of the conditionally averaged spanwise vorticity $\langle\omega^*\rangle$, where

$$\langle\omega^*\rangle = \frac{\partial\langle V^*\rangle}{\partial x^*} - \frac{\partial\langle U^*\rangle}{\partial y^*} \tag{6}$$

are shown in figures 8(*b*) and 8(*c*) for both the opposing and alternating modes. These contours were obtained with the vorticity detection method but similar results were also obtained with the v-detection method. Note that although $\langle\omega^*\rangle$ (also ω^*) is independent of the choice of convection velocity, there is close similarity between the conditional vorticity contours and the conditional streamline patterns, which require a convection velocity, for the same data (figures 6*a* and 6*b*). Significant levels of $\langle\omega^*\rangle$

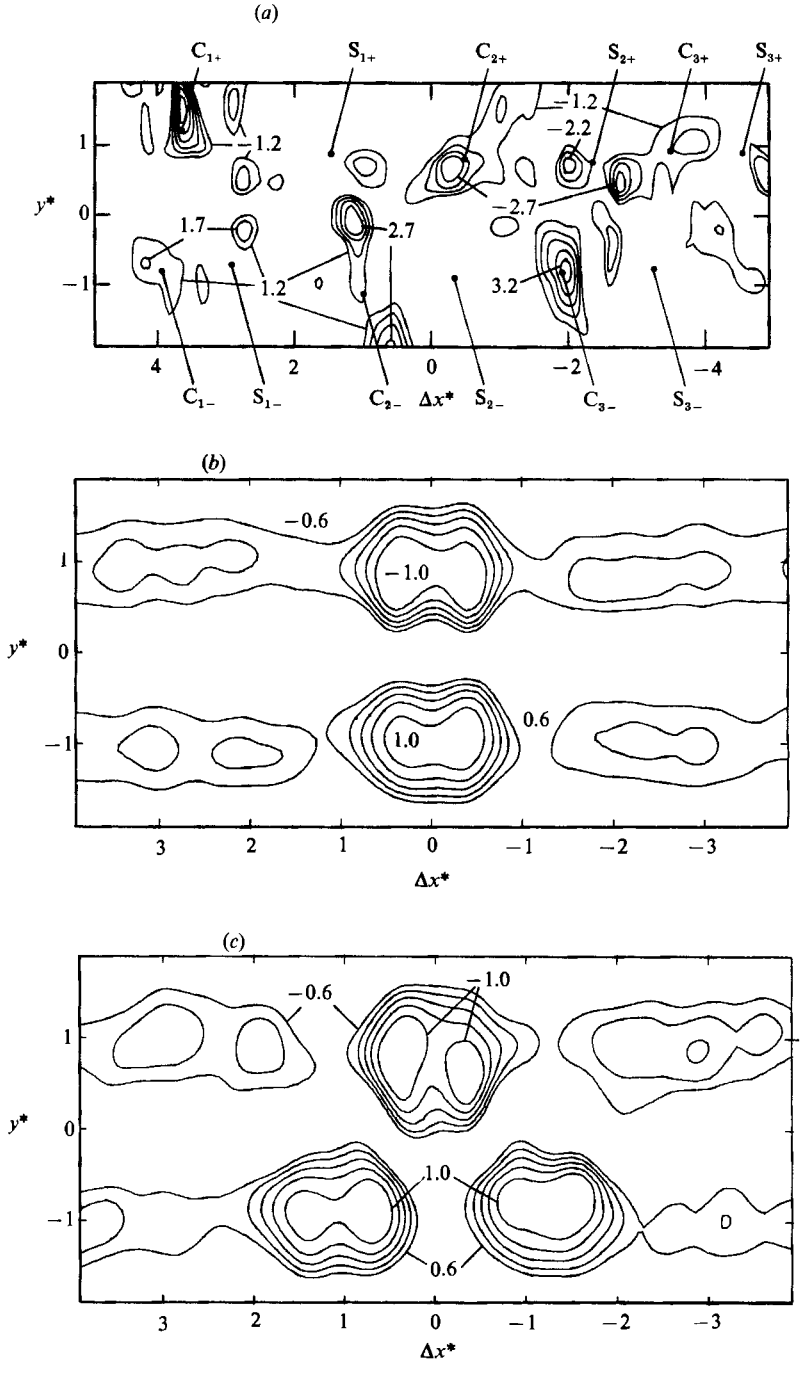

FIGURE 8. Instantaneous and conditionally averaged spanwise vorticity contours. Normalized vorticity values are shown. (*a*) Instantaneous, C and S are the centres/foci and saddles obtained from figure 3; (*b*) conditional for opposing mode (vorticity detection); (*c*) conditional for alternating mode (vorticity detection).

are present throughout the structures in figures 8(*b*) and 8(*c*), consistent with the definition of coherent structures proposed by Hussain (1983, 1986). Figure 8(*a*), however, emphasizes the large variability within and between structures when viewed instantaneously. The widely used approach of generating a single type of conditionally averaged structure based on all detections of reasonably well-defined instantaneous structures may turn out to be an over-simplification, irrespective of the detection method used, whether it be pattern recognition (e.g. Mumford 1983), vorticity detection (e.g. Hussain 1986), WAG (as in the present work), or any other method.

7. Contributions to Reynolds stresses from alternating and opposing modes

It has been shown that the alternating and opposing modes do not occur equally often (figure 5). Consequently, contributions to Reynolds normal stresses ($\overline{u^2}$ and $\overline{v^2}$) and shear stress ($\overline{uv}$) from structures in the two arrangements are also different, but they are generally not in direct proportion to the frequency of occurrence. Contributions were calculated using sets of v-detections, corresponding to either alternating or opposing arrangements of structures, obtained for each probe. For the alternating mode, a detection in the v-signal from a given $\times$-probe was accepted if there were also v-detections at both $\Delta t U_1/L \approx 1.5$ and -1.5 at $|y^*| \approx 0.9$ on the other side of the wake. For the opposing mode, detections were accepted if detections on the other side of the wake at $|y^*| \approx 0.9$ occurred at both $\Delta t U_1/L \approx 3.0$ and 0. The average number of alternating mode detections was 1.91 times the average number of opposing mode detections.

Distributions of $\langle u^2 \rangle$, $\langle v^2 \rangle$ and $\langle uv \rangle$ were calculated for each $\times$-probe in each mode, and then averaged over one structure wavelength ($\Delta x^* \approx 3.0$) using (4), centred on the detection point. The overall properties of the detected regions are compared with Reynolds stresses in figure 9. Values of $\overline{\langle fg \rangle}$ in the figure are calculated from

$$\overline{\langle fg \rangle} = (1.91/2.91)\overline{\langle fg \rangle}_{\text{alternate}} + (1.0/2.91)\overline{\langle fg \rangle}_{\text{opposite}},$$

i.e. each $\overline{\langle fg \rangle}$ is the sum of the values for the two modes weighted in proportion to the frequency of occurrence for each mode. Results for $\overline{\langle v^2 \rangle}$ are a little higher than $\overline{v^2}$ values, probably because detection was based on v-signals, and $\overline{\langle u^2 \rangle}$ is generally a little lower than $\overline{u^2}$. The values of $\overline{\langle uv \rangle}$ and $\overline{uv}$ are quite close. Figure 9 indicates that (for Reynolds stresses at least) the combination of the selected regions of alternating and opposing structures is quite similar to the flow as a whole.

Ratios of the contributions from the alternating and opposing modes to each of the terms of (3), averaged over one structure wavelength, are shown in figure 10. At each $|y^*|$-value the results for the upper and lower sides of the wake are combined. A value of 1.91 indicates that the contribution per detection is the same for the two modes. Results for $\langle f_r g_r \rangle$ (except for the anomalous $\langle u_r^2 \rangle$ at $|y^*| = 2$) are very close to this value (figure 10*c*), as they should be if $\langle f_r g_r \rangle$ is uncorrelated with the detected large-scale structures. Ratios of the large structure contributions are considerably different, however (figure 10*b*). Structures in the alternating mode contribute far more strongly to $\tilde{v}^2$ than to $\tilde{u}^2$, and their contributions to $\tilde{u}\tilde{v}$ are at an intermediate level. Ratios are generally larger towards the centreplane of the wake. The results for $\tilde{v}^2$ are simply explained: structures arranged alternately across the centreline tend to reinforce eaeh other's lateral motion, while structures opposite each other, with

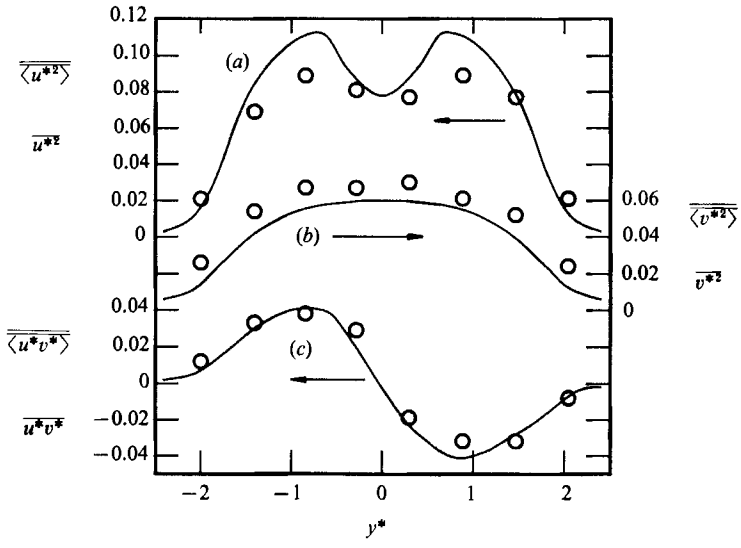

FIGURE 9. Conditionally averaged normal and shear stresses, averaged over one structure length, for the combination of selected regions of alternating and opposing structures. Conventional (long-time averaged) Reynolds stresses are also shown (——): (*a*) $\overline{\langle u^{*2}\rangle}$ and $\overline{u^{*2}}$; (*b*) $\overline{\langle v^{*2}\rangle}$ and $\overline{v^{*2}}$ (*c*) $\overline{\langle u^*v^*\rangle}$ and $\overline{u^*v^*}$.

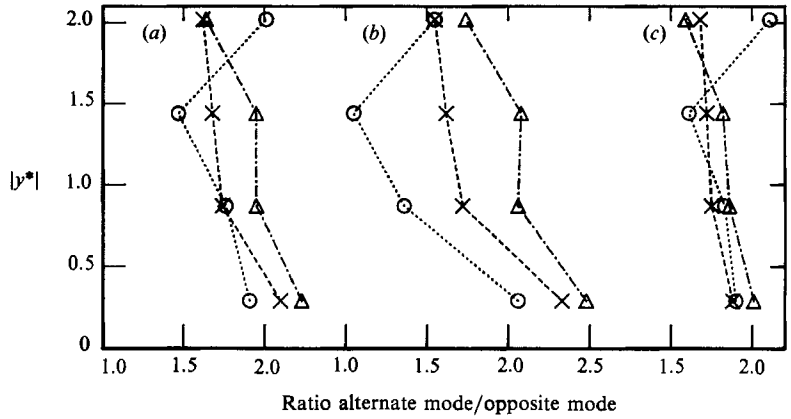

FIGURE 10. Ratios of average contributions to the terms of (3) from the alternating mode to average contributions from the opposing mode: ○, $f = u$, $g = u$; △, v, v; ×, u, v. (*a*) $\langle fg\rangle$ (*b*) $\tilde{f}\tilde{g}$ (*c*) $\langle f_r g_r\rangle$.

opposite directions of rotation, tend to cancel each other's lateral motion. Curves of $\tilde{u}$ (not shown) for the two modes at $|y^*| = 0.87$ and 1.44 indicate that fluid at the upstream ends of large structures opposite each other is significantly lower in streamwise momentum, possibly because of mutual reinforcement of opposite structures in the longitudinal direction. The result is that the ratios of contributions to $\tilde{u}^2$ are comparatively small. Since $\langle fg\rangle$ is the sum of large structure ($\tilde{f}\tilde{g}$) and uncorrelated ($\langle f_r g_r\rangle$) components, the ratios of contributions to $\langle fg\rangle$ from the two modes, shown in figure 10(*a*), always fall between the ratios for the two components (figures 10*b*, *c*).

Spectra of u and v generated from regions containing structures in either

alternating or opposing arrangements were examined, and no significant differences were found. The mean longitudinal velocities for the regions were also very similar.

8. Discrete vortex numerical models of the far wake

Numerical modelling of turbulent flow may be kinematic or dynamic. In the latter case a supercomputer-based numerical solution of some form of the Navier–Stokes equations is usually attempted (see the review article by Rogallo & Moin, 1984, for example) but in the former case a simplified description of the essential features of the flow is usually the main object. Kinematic models such as those presented here can facilitate the analysis and interpretation of experimental results, and could perhaps contribute to vortex dynamics techniques. One aim was to determine the conditions under which large-scale organized motion could be largely responsible for the observed profiles of mean velocity and Reynolds stresses.

The two-dimensional Rankine line vortex was chosen as the basic building block of the models. It has been used by Davies (1976) to model kinematically the planar near wake of a bluff body and by Oler & Goldschmidt (1982) to model kinematically the self-preserving region of the plane jet. The spreading rate of the plane jet is large and was accounted for by Oler & Goldschmidt (1982), while that of the far wake is small and is neglected here.

The equation for the tangential velocity U_θ is

$$U_\theta = \frac{\Gamma}{2\pi r}\{1-\exp[-1.26(r/R_0)^2]\},$$

where Γ is the circulation, r the radial position, and R_0 the cutoff radius (where U_θ is maximum). The unit of length is the mean velocity half-width L, and velocities are scaled so that $U_0 = 1$. A computer program places a number of vortices at specified (x_c, y_c) locations within (or adjacent to) a two-dimensional computational grid, superimposes the U- and V-components of U_θ for each vortex at each grid point, and then calculates $\bar{U}$, $\bar{V}$, $\overline{u^2}$, $\overline{v^2}$ and $\overline{uv}$ as a function of y. For example,

$$\overline{u^2} = \frac{1}{U_0^2 p}\sum_{i=1}^{p}(U_i-\bar{U})^2,$$

where the computational field is p points long (typically 12 points per vortex). The rows of vortices are always extended beyond the computational field so that the data are equivalent to continuous flow. For the results presented here, the longitudinal spacing λ is always equal to the experimental value of 3.0, $|\Gamma|$ is 5.0 (arbitrary) and R_0 is 1.0 for all vortices. The mean transverse velocity $\bar{V}$ is ignored as it is always many orders smaller than $\bar{U}$.

The first model was a series of vortices, with circulation of alternate sign, placed alternately across the centreline at $|y_c| = 0.8$ (figure 11*a*). $\bar{U}(y)$ was correct but the Reynolds stresses were quite wrong, especially $\overline{uv}$ which was virtually zero everywhere. The second model was similar except that the vortices were placed opposite each other (figure 11*b*), but again the stresses were incorrect.

In previous sections, regions of experimental data with either alternating or opposing arrangements of detections were analysed separately, showing differences in the way they contribute to Reynolds stresses. A similar idea was adopted for the third and subsequent models. The third model was simply the sum of the previous

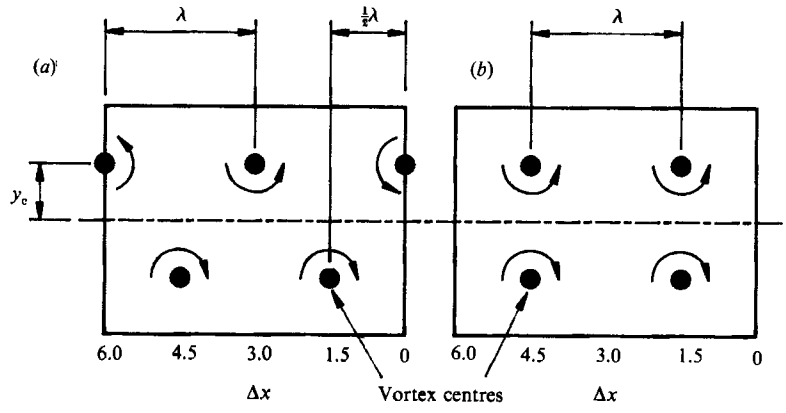

FIGURE 11. Definition sketch for the two arrangements of vortex centre locations in the numerical model of the wake. (*a*) Alternating; (*b*) opposing.

two, in the sense that mean velocity and Reynolds stress profiles were linear combinations of the profiles from the two arrangements of vortices, e.g.

$$\overline{u^2} = \beta \overline{u^2}_{\text{alternate}} + (1-\beta)\,\overline{u^2}_{\text{opposite}}.$$

Values for β in the range 0.6 to 0.7 are indicated by the experimental results (figure 5 and §7). With $\beta = 0.67$, the third model predicts the $\overline{v^2}$ profile quite accurately, but the $\overline{u^2}$ profile is poor and $\overline{uv}$ is still zero.

Velocity fluctuations u and v measured in the potential flow just outside a turbulent wake by Antonia, Shah & Browne (1987*c*) were found to be 90° out of phase. The same result is obtained from the Rankine vortex models, which is the reason why $\overline{uv}$ is zero. Within a turbulent shear flow, however, the phase relationship is generally nearer to 0° or 180° (e.g. Antonia *et al.* 1986), and this aspect was addressed by the fourth model. A phase lag ϕ was introduced into the computation of U, i.e. $U = -U_\theta \sin(\theta - \phi)$, while $V = U_\theta \cos\theta$ as before, where $\theta = \tan^{-1}[(y-y_c)/(x-x_c)]$ for a given point (x, y). The sign of ϕ depends on the sign of Γ, and for $r > R_0$ the value of ϕ is proportional to $(R_0/r)^2$ so that the phase lag occurs only in the 'turbulent' zones. The phase lag is applied to U rather than V because it is found in the experimental data that WAG detections in v-signals from adjacent probes generally occur at the same time while WAG detections in u-signals occur consistently at different times. The fourth model also allows for an additional vortex convection velocity (U_{cc}, V_{cc}) to be applied to the inner regions of the vortices where $r < R_0$, and reduced in proportion to $(R_0/r)^2$ elsewhere, but (U_{cc}, V_{cc}) is not as important as ϕ. It was found that with $\phi = 35°$ and $(U_{cc}, V_{cc}) = (0.19, 0)$ the profiles of $\overline{U}$, $\overline{v^2}$ and $\overline{uv}$ were reproduced very well, but $\overline{u^2}$ values were still very low. Sectional streamlines computed for this model (similar to figure 14) show the correct pattern of foci and saddles (cf. figures 3*c* and 7), unlike streamlines from the first three models which show patterns of centres and saddles.

It was observed earlier that the apparent distances of large structures from the centreline vary considerably (cf. figure 3*c*), and it has long been known (e.g. Grant 1958) that the conventional autocorrelation coefficient for u remains positive up to large x. The fifth model accounts for these two aspects by systematically varying y_c over groups of six vortices per side, with $0.2 \leqslant |y_c| \leqslant 1.5$ (average 0.8). The variation is antisymmetrical for the group of alternating vortices (figure 12*a*) and symmetrical

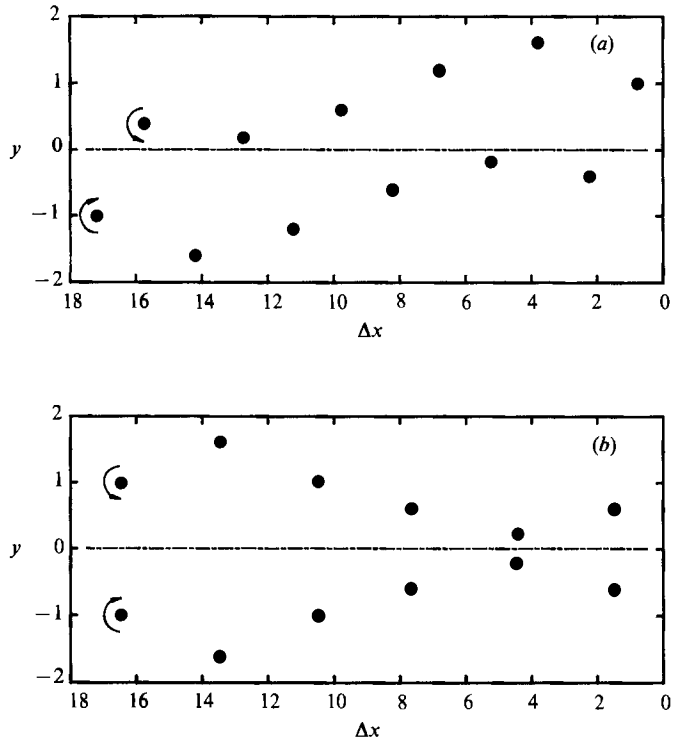

FIGURE 12. Vortex centre locations for the fifth model in which $|y_c|$ is systematically varied. Vortices outside the computation domain are not shown. Note the different scales for Δx and y. (*a*) Alternating mode; (*b*) opposing mode.

for the opposing group (figure 12*b*). The resulting velocity and stress profiles, for parameter values of $\phi = 45°$, $\beta = 0.6$ and $U_{cc} = 0.06$, are compared with measurements (Antonia *et al.* 1987*b*) in figure 13. Agreement is very good, especially for $\overline{v^2}$ and $\overline{uv}$. Note that the profiles for $\overline{u^2}$ and $\overline{v^2}$ from the alternating and opposing groups taken separately are quite different, and it is only their weighted sums that are close to the experimental results. The plane jet model of Oler & Goldschmidt (1982) only considers the alternating mode, and discrepancies in their values of $\overline{u^2}$ and $\overline{v^2}$ near the centreline are similar to the errors that occur if the opposing mode is removed from the present wake model. Sectional streamlines for part of the data are shown in figure 14. It can be inferred from these results that a long-wavelength variation in u, of a scale larger than the largest vortex-like structures, is responsible for both the long positive tail in the measured autocorrelation coefficient and a considerable proportion of the measured $\overline{u^2}$. Townsend (1979) found that vortices tend to travel in groups of three to five with similar characteristics, and the present model is consistent with that result, but there may be other ways besides a systematic variation in y_c of modelling the long-wavelength variation in u.

A kinematic model can be used to examine the performance of detection and conditional averaging procedures developed for use on experimental data. The v-detection algorithm of §3 was applied to data from the fifth model at $y = 0.85$, and, as expected, detected every saddle point between vortices. When the velocities are conditionally averaged, however, there is no accounting for the variation in y_c. Therefore it cannot be expected that the contributions from the conditionally

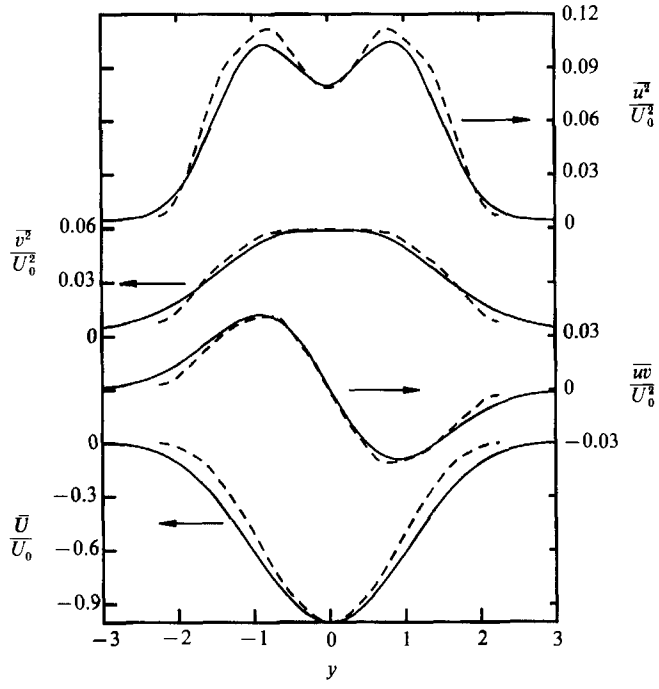

FIGURE 13. Profiles of mean velocity and Reynolds stresses from the model with vortices located as in figure 12, compared to experimental results: ——, model; – –, experiment.

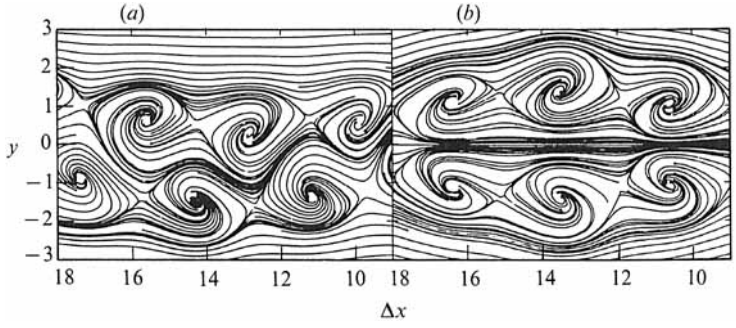

FIGURE 14. Sectional streamlines for part of the data corresponding to figure 12. The frame of reference is translating at $U_1 - 0.5U_0$. (*a*) Alternating mode; (*b*) opposing mode.

averaged structures to $\overline{u^2}$, $\overline{v^2}$ and $\overline{uv}$ (i.e. $\overline{\overline{u^2}/\overline{u^2}}$ etc.) will be exactly 1.0 even though there is no modelling of small-scale turbulence. The values found for the contributions over a range of y were 0.6–0.9 for $\overline{v^2}$, 0.6–1.1 for $\overline{uv}$, but only 0.15–0.3 for $\overline{u^2}$. Experimental values (Antonia *et al.* 1987*b*) are about half of these values. Clearly a more sophisticated detection procedure applied to the model data would result in contributions close to 1.0, and it may be inferred that the experimental values would also be much higher in that case.

As indicated in §5, the magnitude of the divergence $\partial U/\partial x + \partial V/\partial y$ is often significant in the experimental data. The divergence for the first three models was everywhere zero, but significant values were found for the fourth and fifth models with $\phi \neq 0$. Since $\partial U/\partial x + \partial V/\partial y = -\partial W/\partial z$ for incompressible flow, the fourth and fifth models are, therefore, three-dimensional in the sense that they imply that the

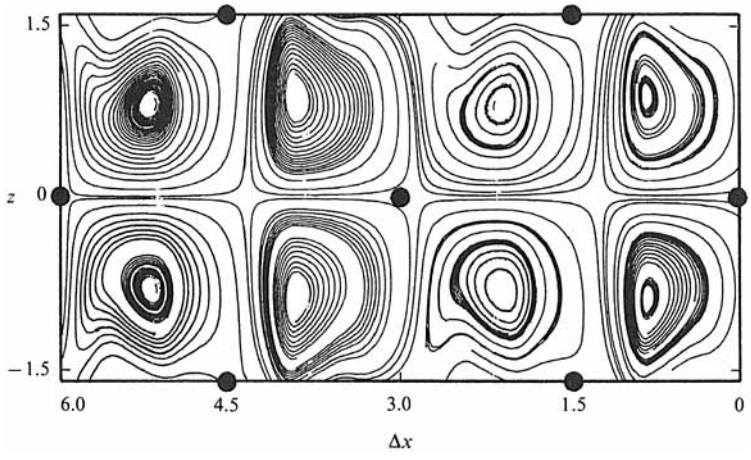

FIGURE 15. Sectional streamlines in the (x,z)-plane at $y = 1.0$ calculated from the quasi-three-dimensional model via the continuity equation. Vortex centres in the three (x,y)-planes are indicated by ●.

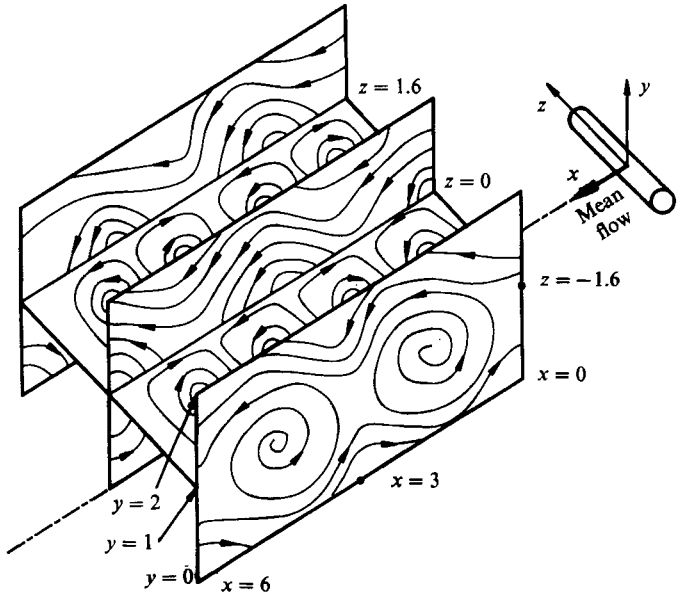

FIGURE 16. Sketch of the inter-relationship between sectional streamlines in the (x,z)- and (x,y)-planes for the quasi-three-dimensional model. Only the upper half of the wake is shown.

spanwise velocity gradient $\partial W/\partial z$ is generally not zero. Grant (1958) and others have found that the correlation between u-measurements separated in the z-direction is significantly negative at $\Delta z \approx 1.6L$, which means that the axes of large spanwise structures are limited in length and/or generally at a considerable angle to the z-axis. By assuming that structure axes are often limited in length, it was possible to construct a simple quasi-three-dimensional model based on the fourth model described above. Three (x,y)-planes containing modified Rankine vortices were placed at three different z-values. One plane was aligned so that one vortex was located at $(x_c, y_c, z_c) = (0, 0.8, 0)$, while the other planes were displaced half a structure wavelength in x and $\pm 1.6L$ in z, i.e. a vortex was centred at $(x_c, y_c, z_c) =$

$(1.5, 0.8, \pm 1.6)$. Velocity components U and V were calculated throughout the three planes, and then calculated at other z values by linear interpolation between the planes. (The implied physical picture is a pattern of interlocking spindle shapes rotating about axes of length $3.2L$ parallel to the z-axis). It was assumed that the $(x, y, 0)$-plane was a plane of symmetry, i.e. $W = 0$ in this plane, and then W was calculated elsewhere by numerical integration of $\partial W = -(\partial U/\partial x + \partial V/\partial y)\,\partial z$.

Sectional streamlines calculated from U and W in the plane $(x, 1.0, z)$ are shown in figure 15 in a frame of reference moving with the mean velocity of that plane. Very similar results were obtained over a large range of y-values provided that the local $\bar{U}$ was used for the frame-of-reference velocity. The pattern in figure 15 conforms remarkably well to the concept of counter-rotating double rollers with axes nearly normal to the centreline of the wake proposed by Grant (1958) and Mumford (1983). The relationship between the (x, z)-plane of figure 15 and the three (x, y)-planes from which it was generated is shown in figure 16. Three-dimensional streamlines resulting from these data would be quite complex. Note that the double-roller pattern does not appear when the U phase delay ϕ is zero, i.e. the model implies that spanwise vortices and double rollers are interlinked through the Reynolds shear stress associated with large-scale organized motion.

9. Conclusions

The velocity signals from an array of eight $\times$-probes were used to 'visualize' the instantaneous motion in the (x, y)-plane of the self-preserving far wake of a cylinder. Vector plots, contours of an approximate stream function, and sectional streamlines, in a translating frame of reference, show a succession of large spanwise vortices (described topologically as a series of saddles and centres/foci) on each side of the wake.

The structures on either side of the centreline may be arranged alternately or directly opposite each other, or in any intermediate arrangement. The alternating arrangement occurs nearly twice as often as the opposing one. Two detection methods which focus on different features of the structures give essentially the same results for the probability distribution of the various modes as well as for other properties of the structures.

Contributions to Reynolds stresses $\overline{u^2}$, $\overline{v^2}$ and $\overline{uv}$ from regions with alternating or directly opposing arrangements of vortices were compared. The biggest differences between them are due to the greater frequency of occurrence of the alternating arrangement. The alternating arrangement is relatively more important for its coherent structure contributions to $\overline{v^2}$ than to $\overline{u^2}$, and the contrast between the two arrangements is generally greatest near the centreline.

Although a simple kinematic model based on the Rankine vortex cannot represent all aspects of a turbulent shear flow, a model that incorporates modified Rankine vortices in both alternating and opposing modes reproduces many flow properties quite well. The success of the model provides, in turn, some justification for a 'coherent structure' approach to the analysis of experimental data. Results from both experiment and model imply that variability in spatial arrangement of structures is an essential flow property. A phase delay in the calculation of the U-component generated by each vortex is required in order to obtain the correct profile of $\overline{uv}$ from the model. A quasi-three-dimensional version of the model implies that large spanwise vortices and double-roller structures, inferred from observations in the (x, z)-plane, may be two views of the same rather complicated three-dimensional

structure. This structure can only exist when the average value of $\tilde{u}\tilde{v}$ (the coherent component of $\overline{uv}$) is non-zero.

The support of the Australian Research Council is gratefully acknowledged.

Appendix

A.1. *Iteration process for approximate two-dimensional stream function*

The stream function approximation is generated as an array $\psi_{i,j}$, where subscript i corresponds to the x-direction and j to the y-direction, for which it is desired that $\partial\psi/\partial y \approx U$ and $\partial\psi/\partial x \approx = -V$. The discrete form of the first equation is $(\psi_{i,j+1}-\psi_{i,j}+E)/\Delta y = \frac{1}{2}(U_{i,j+1}+U_{i,j})$, where E is the approximation error, and similarly for the second equation. After several passes through the data in the $+x$-, $+y$-, $-x$- and $-y$-directions during which values of $\psi_{i,j}$ are altered to reduce E, $\Delta\psi_{i,j}(\max)$ (the largest change in any element) and $\psi_{\mathrm{R}} = \psi_{i,j}(\max)-\psi_{i,j}(\min)$ (the range of the data) are determined. The computation is halted when $\Delta\psi_{i,j}(\max)/\psi_{\mathrm{R}}$ is sufficiently small (i.e. 0.001).

A.2. *Calculation of sectional streamlines using discrete data*

A typical method of evaluating equations (5) is to use a predictor-corrector scheme with velocities between the grid points interpolated using splines or polynomials fitted in two directions (Perry & Steiner 1987). The present scheme differs in that a streamline is moved from its intersection with one grid line to its intersection with another in a single step. Mallinson (1987) reports a different implementation of the single-step idea.

The grid box formed by adjacent grid lines should be reasonably square, so, if necessary, extra grid points are generated (prior to streamline computation) by interpolation in the y-direction. The grid spacing $\Delta x = -U_{\mathrm{c}}\Delta t$ will normally be sufficiently small since Δt is small for a suitable sampling frequency. It is then assumed that velocities vary linearly across each grid box, which is generally a good approximation except when very close to critical points, and is equivalent to assuming a constant acceleration between successive intersections with grid lines. The assumption of a frozen field of vectors means that pathlines are identical to streamlines. It can be shown that a particle of fluid entering a grid box with velocity $\boldsymbol{v}_1$ and undergoing constant acceleration to $\boldsymbol{v}_2$ at the exit point for a time ΔT, and a particle travelling at constant $\boldsymbol{v}_1$ for a time $\frac{1}{2}\Delta T$ and then at $\boldsymbol{v}_2$ for $\frac{1}{2}\Delta T$, have the same point of exit from the grid box. Therefore it is sufficient to find an exit point $\boldsymbol{r}_2 = (x_2, y_2)$ such that

$$\frac{|\boldsymbol{r}_i-\boldsymbol{r}_1|}{|\boldsymbol{v}_1|} = \frac{|\boldsymbol{r}_2-\boldsymbol{r}_i|}{|\boldsymbol{v}_2|},$$

where $\boldsymbol{r}_i$ is the position vector of the intersection between $\boldsymbol{v}_1$ and $\boldsymbol{v}_2$ and $\boldsymbol{r}_1 = (x_1, y_1)$ is the entry point, as shown in figure 17. Since either x_2 or y_2 is known, depending on which side of the current grid box is being tested, the components of $\boldsymbol{v}_2$ are functions of either y_2 or x_2 alone by linear interpolation between the known velocities at the grid points. Therefore the unknown component of $\boldsymbol{r}_2$ can be determined algebraically. If (i) $\boldsymbol{r}_2$ is located between the end points of the side currently being tested; (ii) the sense of $\boldsymbol{v}_2$ is outwards from the box; and (iii) $\boldsymbol{r}_{\mathrm{i}}$ lies within the current box, the point $\boldsymbol{r}_2$ is accepted as a valid continuation of the streamline. Successive sides of a grid box are tested until the criteria are satisfied. The plotted line is slightly smoothed.

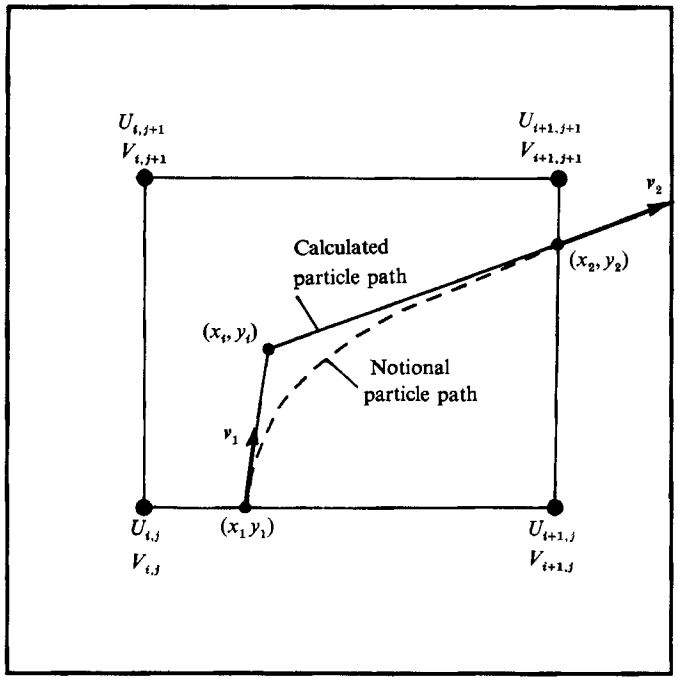

FIGURE 17. Grid box for sectional streamline computations.

Occasionally a streamline is terminated unexpectedly at an ordinary point rather than a critical point. The discrete form of the computation is not designed for the cases where four adjacent velocity vectors are either very different in direction or else exactly parallel, and condition (iii) above may be difficult to satisfy in such cases.

REFERENCES

ANTONIA, R. A., BROWNE, L. W. B. & BISSET, D. K. 1987*a* Symmetric and antisymmetric modes in the turbulent far-wake. *Proc. Sixth Symp. on Turbulent Shear Flows, Toulouse*, pp. 3-10-1–3-10-5.

ANTONIA, R. A., BROWNE, L. W. B., BISSET, D. K. & FULACHIER, L. 1987*b* A description of the organized motion in the turbulent far-wake of a cylinder at low Reynolds number. *J. Fluid Mech.* **184**, 423–444.

ANTONIA, R. A., CHAMBERS, A. J., BRITZ, D. H. & BROWNE, L. W. B. 1986 Organized structures in a turbulent plane jet: topology and contributions to momentum and heat transport. *J. Fluid Mech.* **172**, 211–229.

ANTONIA, R. A. & FULACHIER, L. 1986 Flow visualisation in the turbulent wake of a cylinder. *Rep.* T.N. FM 86/4. Department of Mechanical Engineering, University of Newcastle, NSW.

ANTONIA, R. A., SHAH, D. A. & BROWNE, L. W. B. 1987*c* The organized motion outside a turbulent wake. *Phys. Fluids* **30**, 2040–2045.

BROWNE, L. W. B. & ANTONIA, R. A. 1986 Reynolds shear stress and heat flux measurements in a cylinder wake. *Phys. Fluids* **29**, 709–713.

BROWNE, L. W. B., ANTONIA, R. A. & BISSET, D. K. 1986 Coherent structures in the far-field of a turbulent wake. *Phys. Fluids* **29**, 3612–3617.

CIMBALA, J. M. 1984 Large structure in the far wake of two-dimensional bluff bodies. Ph.D. thesis, California Institute of Technology.

CIMBALA, J. M. 1985 An experimental study of large structures in the far wakes of two-dimensional bluff bodies. *Proc. Fifth Symp. on Turbulent Shear Flows, Cornell University, New York*, pp. 4.1–4.6.

CIMBALA, J. M., NAGIB, H. M. & ROSHKO, A. 1988 Large structure in the far wakes of two-dimensional bluff bodies. *J. Fluid Mech.* **190**, 265–298.

DAVIES, M. E. 1976 A comparison of the wake structure of a stationary and oscillating bluff body, using a conditional averaging technique. *J. Fluid Mech.* **75**, 209–231.

FERRÉ I VIDAL, J. A. 1986 Aplicacio d'algoritmes d'intel-ligencia artificial al reconeixement d'estructures coherents en els fluxos turbulents. Ph.D. thesis, University of Barcelona, Facultad de Quimica, Tarragona.

GRANT, H. L. 1958 Large eddies of turbulent motion. *J. Fluid Mech.* **4**, 149–190.

HAYAKAWA, M. & HUSSAIN, A. K. M. F. 1985 Eduction of coherent structures in the turbulent plane wake. *Proc. Fifth Symp. on Turbulent Shear Flows, Cornell University*, pp. 4.33–4.38.

HUSSAIN, A. K. M. F. 1983 Coherent structures – reality and myth. *Phys. Fluids* **26**, 2816–2850.

HUSSAIN, A. K. M. F. 1986 Coherent structures and turbulence. *J. Fluid Mech.* **173**, 303–356.

KEFFER, J. F. 1965 The uniform distortion of a turbulent wake. *J. Fluid Mech.* **22**, 135–159.

MALLINSON, G. D. 1987 The calculation of the lines of a 3-dimensional vector field. Presented at the *2nd Intl Symp. Comput. Fluid Dynamics, Sydney*.

MUMFORD, J. C. 1983 The structure of the large eddies in fully turbulent shear flows. Part 2. The plane wake. *J. Fluid Mech.* **137**, 447–456.

OLER, J. W. & GOLDSCHMIDT, V. W. 1981 Coherent structures in the similarity region of two-dimensional turbulent jets. *Proc. Third Symp. on Turbulent Shear Flows, University of California at Davis*, pp. 11.1–11.6.

OLER, J. W. & GOLDSCHMIDT, V. W. 1982 A vortex-street model of the flow in the similarity region of a two-dimensional free turbulent jet. *J. Fluid Mech.* **123**, 523–535.

PAPAILIOU, D. D. & LYKOUDIS, P. S. 1974 Turbulent vortex streets and the entrainment mechanism of the turbulent wake. *J. Fluid Mech.* **62**, 11–31.

PERRY, A. E. & CHONG, M. S. 1987 A description of eddying motions and flow patterns using critical-point concepts. *Ann. Rev. Fluid Mech.* **19**, 125–155.

PERRY, A. E. & STEINER, T. R. 1987 Large-scale vortex structures in turbulent wakes behind bluff bodies. Part 1. Vortex formation processes. *J. Fluid Mech.* **174**, 233–270.

ROGALLO, R. S. & MOIN, P. 1984 Numerical simulation of turbulent flows. *Ann. Rev. Fluid Mech.* **16**, 99–137.

TANEDA, S. 1959 Downstream development of the wakes behind cylinders. *J. Phys. Soc. Japan* **14**, 843–848.

THOMAS, F. O. & GOLDSCHMIDT, V. W. 1986 Structure characteristics of a developing turbulent plane jet. *J. Fluid Mech.* **163**, 227–256.

TOWNSEND, A. A. 1979 Flow patterns of large eddies in a wake and in a boundary layer. *J. Fluid Mech.* **95**, 515–537.

WLEZIEN, R. W. 1981 The evolution of the low wavenumber structure in a turbulent wake. Ph.D. thesis, Illinois Institute of Technology.

WYGNANSKI, I., CHAMPAGNE, F. & MARASLI, B. 1986 On the large-scale structures in two-dimensional, small-deficit, turbulent wakes. *J. Fluid Mech.* **168**, 31–71.

WYGNANSKI, I. J. & PETERSEN, R. A. 1987 Coherent motion in excited free shear flows. *AIAA J.* **25**, 201–213.